Available online at www.sciencedirect.com
SCIENCE DIRECT®
International Journal of Heat and Mass Transfer 49 (2006) 2315–2327
International Journal of HEAT and MASS TRANSFER
www.elsevier.com/locate/ijhmt

Heat/mass transfer in porous electrodes of fuel cells

J.J. Hwang *, P.Y. Chen

Research Center for Advanced Science and Technology, Mingdao University, Changhua 52345, Taiwan

Received 21 December 2004
Available online 28 February 2006

Abstract

This paper has provided an innovative aspect in the heat/mass transfer of fuel-cell related studies. A heat/mass coupled modeling approach is presented to predict the transport phenomena inside the porous electrode of a fuel cell. The energy equations based on the local thermal non-equilibrium (LTNE) are derived to resolve the temperature difference between the solid and fluid phases inside the porous electrode. The surface heat transfer is coupled with the species transports via a macroscopic electrochemical model on the reaction boundary. First, a general criterion for the local thermal non-equilibrium in porous electrodes is proposed in terms of non-dimensional parameters of engineering importance. Then, the significance of local thermal non-equilibrium in a typical porous electrode is assessed. Furthermore, detailed distributions of the local temperature, local Nusselt number, species concentration, and electric current density inside the porous electrode of fuel cells are presented. Finally, the effect of LTNE parameters on the thermal-fluid behaviors in the porous electrode is investigated.

Keywords: Local thermal non-equilibrium (LTNE); Fuel cells; Porous electrodes; Transport phenomena

1. Introduction

It is known that temperature variations inside a fuel cell significantly affect its performance, lifetime, and reliability [1,2]. In order to prolong the fuel cell, balanced utilization of active materials is required to avoid local degradation, which needs a highly uniform temperature profile inside the fuel cell. In addition, the fuel cell temperature may increase greatly due to the exothermic electrochemical reactions in the porous electrode. The thermal runaway may be triggered by the hot spots on the reaction surfaces of the electrode. Therefore, a proper thermal management is required for safely operating a fuel cell, which not only optimizes the operating temperature range but also keeps a high uniformity of the internal temperature distribution. However, the small temperature differences between the fuel cell and the environment make thermal management a challenging problem. That is an excessive heat produced by the electrochemical reaction should be removed totally and evenly by a limited temperature difference.

Because of the highly reactive environment and compact nature of a fuel cell it is hard to perform detailed in situ measurements during operation. Such information has been sought through modeling or simulation to improve understanding of transport phenomena inside a fuel cell. Numerous fuel-cell models have been developed accounting for various physical processes in the past two decades. Most regarded the electrochemical reaction as an isothermal process, and did not consider thermal transports [3–11]. The emerging fields of thermal transport in a fuel cell, however, did not receive attention to the same extent. Only several analytical/numerical models studied the thermal-fluid transport in the porous electrode based on the local thermal equilibrium (LTE) [12,13]. Under the assumption of local thermal equilibrium, both fluid and solid in the porous electrode have the same temperatures. The so-called one-equation approach [14–17] is employed to obtain

* Corresponding author. Tel.: +886 48876660x1500; fax: +886 422518272.
E-mail address: azaijj@mdu.edu.tw (J.J. Hwang).

0017-9310/$ - see front matter © 2006 Elsevier Ltd. All rights reserved.
doi:10.1016/j.ijheatmasstransfer.2005.11.021

Nomenclature

A	front area of the module inlet per unit length (m)
A_R	reaction surface area per unit length (m)
a_1, a_2	coefficients in Eq. (45)
a_s	total surface area in the porous electrode (m^2)
Bi	Biot number
d	pore diameter of the porous medium (m)
c_{H_2O}	water vapor mole concentration (mol m^{-3})
$c_{H_2O,ref}$	water vapor mole concentration at inlet (mol m^{-3})
C_{H_2O}	normalized water vapor concentration, c_{H_2O}/c_{tot}
$C_{H_2O,ref}$	normalized water vapor mole concentration at inlet, $c_{H_2O,ref}/c_{tot}$
c_{O_2}	oxygen concentration (mol m^{-3})
$c_{O_2,ref}$	oxygen mole concentration at inlet (mol m^{-3})
C_{O_2}	normalized oxygen concentration, c_{O_2}/c_{tot}
$C_{O_2,ref}$	normalized oxygen mole concentration at inlet, $c_{O_2,ref}/c_{tot}$
c_p	specific heat at constant temperature (J kg^{-1} K^{-1})
c_{tot}	total mole concentration of the reacting fluid (mol m^{-3})
D_{H_2O}	binary diffusivity of water vapor in the oxygen (m^2 s^{-1})
$D_{H_2O,eff}$	effective diffusivity of water vapor in the gas diffusion layer (m^2 s^{-1})
D_{O_2}	binary diffusivity of oxygen in the water vapor (m^2 s^{-1})
$D_{O_2,eff}$	effective diffusivity of oxygen in the gas diffusion layer (m^2 s^{-1})
Da	Darcy number
Ec_1, Ec_2	coefficients in Eq. (40)
F	Faraday's constant (96487 C mol^{-1})
h_v	interstitial heat transfer coefficient (W m^{-3} K^{-1})
i	local current density (A m^{-2})
k	thermal conductivity (W m^{-1} K^{-1})
L	length of the computational domain (m)
$\dot{m}$	mass transfer rate (kg s^{-1})
p	pressure (Pa)
P	non-dimensional pressure
Pr	Prandtl number
q	local heat transfer rate (W m^{-2})
Q	total heat transfer from the system (W)
Re	Reynolds number
R_k	fluid-to-solid conductivity ratio
R_{M1}, R_{M2}	coefficients in Eq. (29)
R_{N1}, R_{N2}	coefficients in Eq. (30)
S_V	surface area-to-volume ratio (m^{-1})
Sc	Schmidt number
T	temperature (K)
u, v	velocity components in the x, and y directions, respectively (m s^{-1})
U, V	non-dimensional velocity components in the x, and y direction
x, y	coordinate system (m)
X, Y	non-dimensional x and y coordinate

Greek symbols

α_1, α_2	coefficients in Eq. (23)
δ	thickness of the porous electrode (m)
ε	porosity of the porous electrode
κ	permeability of the porous electrode (m^2)
ρ	density (kg m^{-3})
η	cathodic overpotential (V)
θ	non-dimensional temperature
ϕ_s	solid-phase electric potential (V)
σ	electric conductivity (S m)
τ	tortuosity of the porous electrode
Φ_s	non-dimensional solid-phase electric potential

Subscripts

eff	effective
f	fluid phase
in	inlet
loc	local
o	oxygen
out	outlet
r or ref	reference
s	solid phase
SYS	system
tot	total

temperature distributions in the porous electrode. In practical applications, however, the temperature difference between the inlet and the outlet of a low-temperature fuel cell (such as PEMFC, proton exchange membrane fuel cell) is not large. In addition, the conductivities of the solid matrix (such as carbon fibers) and the reactant fluid (such as air) are quite different. That is the temperature between the solid and the fluid phases may be different and thus away from the local thermal equilibrium.

In the present study, a multi-physics model coupling heat/mass transfer with electrochemical kinetics is developed to simulate the transport phenomena inside the porous electrode of a low-temperature fuel cell. An LTNE parameter is proposed to examine the extent of local thermal non-equilibrium in a typical fuel cell electrode. Then, numerical simulations based on a local thermal non-equilibrium approach are carried out to study thermal-fluid behaviors of porous electrode under varies LTNE parameters. The present work together with the author's another effort [17] is the first attempt to develop a heat/mass coupled model which is capable of predicting the fluid and solid temperatures inside a fuel cell simultaneously.

2. Criterion of local thermal non-equilibrium

Before undertaking the modeling, a preliminary analysis using order-of-magnitude is conducted to assess the validation of the assumption of local thermal equilibrium in the porous electrodes of fuel cells. Each temperature in the porous electrode is depicted in Fig. 1. If the local thermal equilibrium is valid, the temperature difference between the solid phase (T_s) and the fluid phase (T_f) in a representative elementary volume (REV) of the porous electrode is much smaller than that occurring over the system [18–20], i.e.,

$$\Delta T_{\mathrm{loc}} \ll \Delta T_{\mathrm{SYS}} \tag{1}$$

where $\Delta T_{\mathrm{SYS}} = |T_{\mathrm{f.out}} - T_{\mathrm{f,in}}|$ and $\Delta T_{\mathrm{loc}} = |T_s - T_f|$. Conversely, the local thermal non-equilibrium becomes significant as they have the same order, i.e.,

$$\mathrm{O}\left[\frac{\Delta T_{\mathrm{loc}}}{\Delta T_{\mathrm{SYS}}}\right] \sim 1 \tag{2}$$

In low-temperature fuel cells such as PEMFCs, the typical temperature difference (ΔT_{SYS}) between the cell inlet and outlet is only about 30–50 °C. Thus, a little temperature difference between the two phases may cause a significant local thermal non-equilibrium inside the porous electrode.

The local heat flux in the REV is

$$q \sim h_v \Delta T_{\mathrm{loc}}/S_V \tag{3}$$

where h_v is the interstitial heat transfer coefficient between the fluid and solid phases, and S_V is the interfacial surface area per unit volume. Then, the total heat transfer rate from solid phase to fluid phase in the system can be expressed as

$$Q \sim a_s \cdot (h_v \Delta T_{\mathrm{loc}}/S_V) \tag{4}$$

where a_s total wetted surface area in the porous electrode.

It is assumed that the heat transfer rate from the solid phase to the fluid phase in the porous electrode is equal to the heat transfer rate which is carried by the fluid flowing through the porous electrode. Therefore, from the system viewpoint, the total heat transfer rate can be expressed as

$$Q \sim \dot{m} c_p \Delta T_{\mathrm{SYS}} \tag{5}$$

where $\dot{m}$ is the mass flow rate of the reactants and can be expressed as $\dot{m} = \rho \varepsilon a_s/(S_V t)$. Each temperature difference is obtained from Eqs. (4) and (5) as

$$\Delta T_{\mathrm{loc}} \sim \frac{Q}{h_v a_s/S_V} \tag{6}$$

$$\Delta T_{\mathrm{SYS}} \sim \frac{Q}{(\rho c_p)_f \varepsilon a_s/(S_V t)} \tag{7}$$

Therefore, the degree of the local thermal equilibrium (or non-equilibrium) in the porous electrode is expressed as

$$\mathrm{O}\left[\frac{\Delta T_{\mathrm{loc}}}{\Delta T_{\mathrm{SYS}}}\right] \sim \frac{(\rho c_p)_f \varepsilon}{h_v t} \tag{8}$$

The time scale t shown in the above equation as well as in the mass flow rate ($\dot{m}$) is represented by $t = \delta/u_d$, where δ and u_d are the electrode thickness (a characteristic length) and pore velocity, respectively. It means the time requirement for flow traversing the porous electrode from the module inlet to the active surfaces. The interstitial heat transfer coefficient can be expressed by

$$h_v = \frac{Bi \cdot k_{s,\mathrm{eff}}}{\delta^2} \tag{9}$$

where Bi is the Biot number of the solid matrix immersed in the reactant fluid of the porous electrode. By substituting Eq. (9) into Eq. (8) and using the following non-dimensional parameters:

$$Pr_{\mathrm{eff}} = \frac{\mu (c_p)_f}{k_{f,\mathrm{eff}}}, \quad Re = \frac{u_d \delta}{v} \quad \text{and} \quad R_k = \frac{k_{f,\mathrm{eff}}}{k_{s,\mathrm{eff}}} \tag{10}$$

the degree of local thermal equilibrium is presented by a non-dimensional form

$$\mathrm{O}\left[\frac{\Delta T_{\mathrm{loc}}}{\Delta T_{\mathrm{SYS}}}\right] \sim \varepsilon Pr_{\mathrm{eff}} Re R_k / Bi \tag{11}$$

where Pr_{eff}, Re, and R_k are the Prandtl number, the Reynolds number, and the fluid-to-solid conductivity ratio, respectively.

From Eq. (11), the significance of local thermal non-equilibrium in a porous electrode increases as the LTNE parameter $\varepsilon Pr_{\mathrm{eff}} Re R_k/Bi$ approaches unit. In contrast, it becomes the local thermal equilibrium for $\varepsilon Pr_{\mathrm{eff}} Re R_k/Bi \ll 1$.

Up to the present time, the interstitial heat transfer coefficient (h_v in Eqs. (3) and (4)) of porous electrodes of a fuel cell has not been measured yet in the open literature. The fuel cell electrode consists of carbon-fiber matrices. In morphology, it is somewhat like the aluminum foam. Therefore, the data of interstitial heat transfer coefficient obtained for the aluminum form is employed in the present prediction. From the h_v correlation of aluminum foams measured by using the single-blowing technique [19],

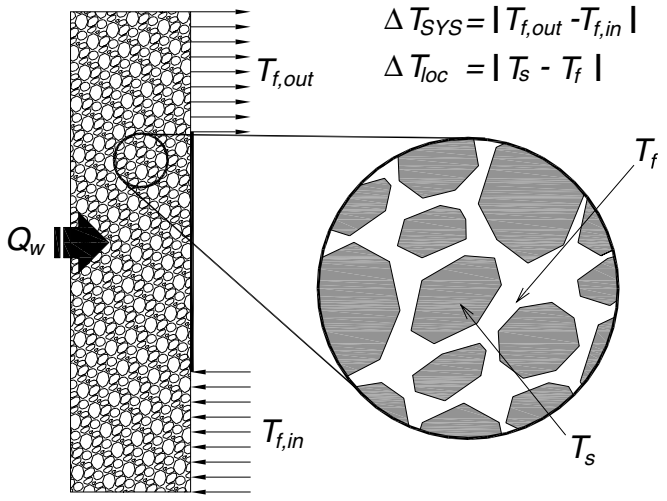

Fig. 1. Schematic drawing of the local thermal non-equilibrium in the porous electrode.

Table 1
Porous electrode data sheet

Property name	Solid phase	Fluid phase
Physical properties[a]		
Material	Carbon fiber	Oxygen
Bulk density, ρ	1100 kg m^{-3}	1.13 kg m^{-3}
Specific resistance, σ^{-1}	115 μΩ m	–
Thermal conductivity, k	1.71 W m^{-1} K^{-1}[b]	0.0268 W m^{-1} K^{-1}
Coefficient of thermal expansion, β	9.0×10^{-7} K^{-1}	3.33×10^{-3} K^{-1}
Viscosity, ν	–	1.586×10^{-5} m^2 s^{-1}
Thermal diffusivity, α_f	–	2.235×10^{-5} m^2 s^{-1}
Geometric properties		
Porosity, ε	48%	
Thickness of the electrode, δ	400 μm	
Tortuosity of the electrode, τ	1.5	
Average pore diameter, d	33 μm	
Permeability (O_2), κ[c]	1.57×10^{-12} m^2	
Flow properties		
Volumetric heat transfer coefficient, h_v	1.0×10^{6} W m^{-3} K^{-1} (baseline case, assumed)	
Pore velocity, u_d for $I(iA_R)=1$ A at stoichiometric flow ratio of 5	0.239 m s^{-1}	
Non-dimensional parameters		
Conductivity ratio, R_k	0.01447	
Prandtl number, Pr	0.709	
Reynolds number, Re	6	
Biot number, Bi	0.1799	
$\varepsilon PrReR_k/Bi$	0.1644	

[a] Data from manufacture.
[b] Oxygen at 25 °C with 15% RH, $p=0.15$ atm, plate thickness: 2.5 cm, 51 L/m^2 s.
[c] ASTM E1530.

it varies from $3.0\times10^4 \leqslant h_v \leqslant 1.5\times10^5$ W m^{-3} K^{-1} for $0.7<\varepsilon<0.95$. Results also show that h_v increases with decreasing the porosity. Accordingly, the interfacial heat transfer coefficient for the base-line case in the present study is assumed to be $h_v=1.0\times10^6$ W m^{-3} K^{-1} for $\varepsilon=0.5$. Table 1 summarized the physical, geometric and flow prosperities of a typical PEMFC. With an assumption of $h_v=1.0\times10^6$ W m^{-3} K^{-1}, the value of the parameter $\varepsilon Pr_{\text{eff}}ReR_k/Bi$ is about 0.1644, which is large enough to ensure the local thermal non-equilibrium in the porous electrode of a fuel cell.

3. Numerical model

The schematic drawing of the present model is shown in Fig. 2, which shows a typical module of an interdigitated flow field plate. The computational module has a dimension of 400 μm (width) by 1600 μm (length). In the model, the anodic reaction of a PEMFC is neglected due to its fast kinetics [21], and therefore, only the oxygen reduction reaction (ORR) on the cathode is considered [22], i.e.,

$$O_2 + 4H^+ + 4e^- \leftrightarrow 2H_2O \tag{12}$$

The oxygen–water vapor mixture enters the porous cathode from the module inlet (inlet channel), then transverses the porous electrode to the reaction surfaces. The electrochemical reaction occurs on the reaction surfaces to consume the oxygen (C_{O_2}) and meanwhile produce the water vapor (C_{H_2O}) and the current (I). In addition, a considerable mount of heat (Q_w) is generated on the surfaces by the overpotential heating, and partly by irreversibility. All products and un-reacted reactants either exit from the module outlet or conduct through the rib surfaces.

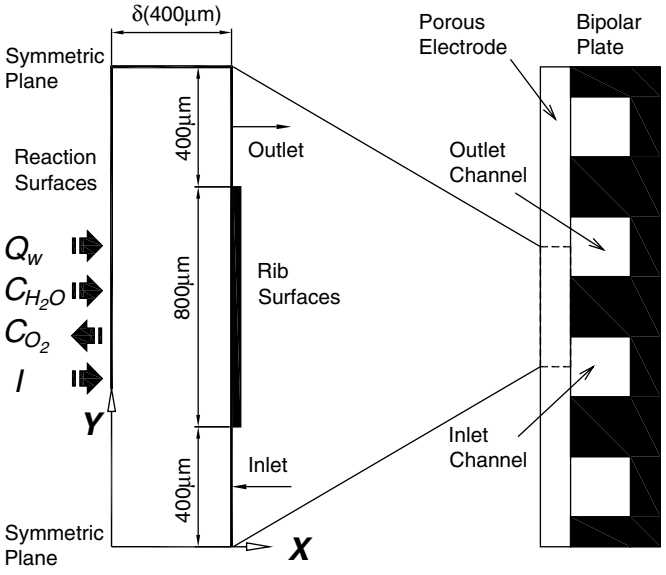

Fig. 2. Configuration of the computational domain.

3.1. Assumptions

The following assumptions are used in this model:

(1) Gas mixtures are ideal gas.
(2) The fluid flow is steady, laminar, and incompressible; its thermal physical properties are constant.
(3) Porous electrode is homogeneous and isotropic with uniform morphological properties such as porosity, tortuosity and permeability.
(4) Water in the electrode exits as vapor only.
(5) Catalyst layer is treated as an ultra-thin layer; thus the oxygen reduction reaction is considered to occur only at the surfaces of the catalyst layer.
(6) The inlet fluid and rib-surface temperatures are uniform.

3.2. Velocity distributions

In the porous electrode, the Brinkman-extended Darcy equations together with the mass conservation are solved to obtain the velocity profiles and pressure distributions.

$$\rho_f u\frac{\partial u}{\partial x}+\rho_f v\frac{\partial u}{\partial y}=-\frac{\partial p}{\partial x}+\mu\left(\frac{\partial^2 u}{\partial x^2}+\frac{\partial^2 u}{\partial y^2}\right)-\frac{\mu}{\kappa}\varepsilon u \tag{13}$$

$$\rho_f u\frac{\partial v}{\partial x}+\rho_f v\frac{\partial v}{\partial y}=-\frac{\partial p}{\partial y}+\mu\left(\frac{\partial^2 v}{\partial x^2}+\frac{\partial^2 v}{\partial y^2}\right)-\frac{\mu}{\kappa}\varepsilon v \tag{14}$$

$$\frac{\partial(\rho_f u)}{\partial x}+\frac{\partial(\rho_f v)}{\partial y}=0 \tag{15}$$

Using the non-dimensional parameters of $u_d=\dfrac{\dot m}{\rho_f A\varepsilon}$, $X=\dfrac{x}{\delta}$, $Y=\dfrac{y}{\delta}$, $U=\dfrac{u}{u_d}$, $V=\dfrac{v}{u_d}$, $P=\dfrac{p}{\rho_f u_d^2}$, $Da=\dfrac{\kappa}{\delta^2}$, and $Re=\dfrac{u_d\delta}{v}$, the above equations are further reduced to dimensionless forms of:

$$U\frac{\partial U}{\partial X}+V\frac{\partial U}{\partial Y}=-\frac{\partial P}{\partial X}+\frac{1}{Re}\left(\frac{\partial^2 U}{\partial X^2}+\frac{\partial^2 U}{\partial Y^2}\right)-\frac{1}{Re\cdot Da}\varepsilon U \tag{16}$$

$$U\frac{\partial V}{\partial X}+V\frac{\partial V}{\partial Y}=-\frac{\partial P}{\partial Y}+\frac{1}{Re}\left(\frac{\partial^2 V}{\partial X^2}+\frac{\partial^2 V}{\partial Y^2}\right)-\frac{1}{Re\cdot Da}\varepsilon V \tag{17}$$

$$\frac{\partial U}{\partial X}+\frac{\partial V}{\partial Y}=0 \tag{18}$$

On the reaction surfaces, $U=0$, $V=0$ and $\dfrac{\partial P}{\partial X}=0$

3.3. Concentration distributions

The species transports of the oxygen and water vapor in the porous cathode can be governed by the following equations:

$$u\frac{\partial c_{O_2}}{\partial x}+v\frac{\partial c_{O_2}}{\partial y}=D_{O_2,\mathrm{eff}}\left(\frac{\partial^2 c_{O_2}}{\partial x^2}+\frac{\partial^2 c_{O_2}}{\partial y^2}\right) \tag{19}$$

$$u\frac{\partial c_{H_2O}}{\partial x}+v\frac{\partial c_{H_2O}}{\partial y}=D_{H_2O,\mathrm{eff}}\left(\frac{\partial^2 c_{H_2O}}{\partial x^2}+\frac{\partial^2 c_{H_2O}}{\partial y^2}\right) \tag{20}$$

where $D_{O_2,\mathrm{eff}}$ and $D_{H_2O,\mathrm{eff}}$ are the effective diffusivities of the oxygen and water vapor in the porous electrode, respectively, which follow the Bruggemann model [23], i.e.,

$$D_{O_2,\mathrm{eff}}=\varepsilon^{\tau}D_{O_2} \tag{21}$$

$$D_{H_2O,\mathrm{eff}}=\varepsilon^{\tau}D_{H_2O} \tag{22}$$

According to the Butler–Volmer correlation [24], the rate of electrochemical reaction on the reaction surfaces can be described by the relationship of the local current density and the reactant concentrations, i.e.,

$$i=i_{rd}+i_{ox}=\alpha_1\left(\frac{c_{O_2}}{c_{O_2,\mathrm{ref}}}\right)-\alpha_2\left(\frac{c_{H_2O}}{c_{H_2O,\mathrm{ref}}}\right)^2 \tag{23}$$

α_1 and α_2 are electrochemical coefficients depending on the exchange current density and the overpotential on the electrode surfaces. They are regarded as constants in the present simulation. The first term of the right-hand side of Eq. (23) is the reductive current representing the strength of forward reaction, while the second term is the oxidative current that has an opposed effect on the oxygen reduction reaction. From Eq. (12), the oxygen consumed rate on the reaction surfaces by the ORR should be equal to the produced current. Therefore, the balance of the oxygen concentration on the reaction boundary becomes

$$-D_{O_2,\mathrm{eff}}\frac{\partial c_{O_2}}{\partial x}=\frac{i}{4F} \tag{24}$$

That is

$$D_{O_2,\mathrm{eff}}\frac{\partial c_{O_2}}{\partial x}+\frac{\alpha_1}{4F}\left(\frac{c_{O_2}}{c_{O_2,\mathrm{ref}}}\right)-\frac{\alpha_2}{4F}\left(\frac{c_{H_2O}}{c_{H_2O,\mathrm{ref}}}\right)^2=0 \tag{25}$$

Similarly, the conservation of water–vapor concentration on the reaction surfaces is

$$D_{H_2O,\mathrm{eff}}\frac{\partial c_{H_2O}}{\partial x}-\frac{\alpha_2}{2F}\left(\frac{c_{H_2O}}{c_{H_2O,\mathrm{ref}}}\right)^2+\frac{\alpha_1}{2F}\left(\frac{c_{O_2}}{c_{O_2,\mathrm{ref}}}\right)=0 \tag{26}$$

By using the following non-dimensional parameters of

$$C_{H_2O}=\frac{c_{H_2O}}{c_{\mathrm{tot}}},\quad C_{H_2O,\mathrm{ref}}=\frac{c_{H_2O,\mathrm{ref}}}{c_{\mathrm{tot}}},\quad C_{O_2}=\frac{c_{O_2}}{c_{\mathrm{tot}}},$$

$$C_{O_2,\mathrm{ref}}=\frac{c_{O_2,\mathrm{ref}}}{c_{\mathrm{tot}}},\quad Sc_{O_2}=\frac{v}{D_{O_2,\mathrm{eff}}},\quad Sc_{H_2O}=\frac{v}{D_{H_2O,\mathrm{eff}}},$$

$$R_{M1}=\frac{\alpha_1\delta}{4Fc_{\mathrm{tot}}D_{O_2,\mathrm{eff}}},\quad R_{M2}=\frac{\alpha_2\delta}{4Fc_{\mathrm{tot}}D_{O_2,\mathrm{eff}}},$$

$$R_{N1}=\frac{\alpha_1\delta}{2Fc_{\mathrm{tot}}D_{H_2O,\mathrm{eff}}},\quad \text{and}\quad R_{N2}=\frac{\alpha_2\delta}{2Fc_{\mathrm{tot}}D_{H_2O,\mathrm{eff}}},$$

the dimensionless forms of the species transport equations can be written as

$$U\frac{\partial C_{O_2}}{\partial X}+V\frac{\partial C_{O_2}}{\partial Y}=\frac{1}{Re\cdot Sc_{O_2}}\left(\frac{\partial^2 C_{O_2}}{\partial X^2}+\frac{\partial^2 C_{O_2}}{\partial Y^2}\right) \tag{27}$$

$$U\frac{\partial C_{H_2O}}{\partial X}+V\frac{\partial C_{H_2O}}{\partial Y}=\frac{1}{Re\cdot Sc_{H_2O}}\left(\frac{\partial^2 C_{H_2O}}{\partial X^2}+\frac{\partial^2 C_{H_2O}}{\partial Y^2}\right) \tag{28}$$

The boundary conditions on the reaction surfaces are

$$\frac{\partial C_{O_2}}{\partial X} + R_{M1} C_{O_2} - R_{M2} (C_{H_2O})^2 = 0 \tag{29}$$

$$\frac{\partial C_{H_2O}}{\partial X} - R_{N2} (C_{H_2O})^2 + R_{N1} C_{O_2} = 0 \tag{30}$$

3.4. Temperature distributions

The energy equations are developed by application of the local volume-average technique. This averaging process may obscure local pore phenomena that contribute to the global transport. Energy equations for the solid and fluid phases are as follows:

$$0 = k_{s,eff} \left(\frac{\partial^2 T_s}{\partial x^2} + \frac{\partial^2 T_s}{\partial y^2} \right) - h_v (T_s - T_f) \tag{31}$$

$$(\rho c_p)_f u \frac{\partial T_f}{\partial x} + (\rho c_p)_f v \frac{\partial T_f}{\partial y} = k_{f,eff} \left(\frac{\partial^2 T_f}{\partial x^2} + \frac{\partial^2 T_f}{\partial y^2} \right) + h_v (T_s - T_f) \tag{32}$$

The effective thermal conductivities of both phases are respectively defined as

$$k_{s,eff} = (1 - \varepsilon) k_s \tag{33}$$

$$k_{f,eff} = \varepsilon k_f \tag{34}$$

On the ORR surfaces, the heat generation by the electrochemical reaction for an isobaric fuel cell system [25] can be represents by

$$q = i\eta + \text{mixing enthalpy change} + \text{phase change enthalpy change} \tag{35}$$

where η is the cathode overpotential. The second term (the enthalpy-of-mixing term) represents the heat effect associated with concentration gradients developed in the cell. The last term stands for the heat transfer due to phase changes. If the enthalpy changes due to the mixing and phase change (the 3rd and 4th terms of Eq. (35)) are neglecting [26], the energy balance at the reaction surfaces can be written as

$$-k_{s,eff} \frac{\partial T_s}{\partial x} - k_{f,eff} \frac{\partial T_f}{\partial x} = i\eta \tag{36}$$

In addition, on the reaction surfaces, the fluid and solid phases have the same temperature, i.e.,

$$T_f = T_s \tag{37}$$

The above equations can be non-dimensionalized by using the non-dimensional variables

$$\theta = \frac{T - T_r}{T_{f,in} - T_r}, \quad Pr_{eff} = \frac{\mu (c_p)_f}{k_{f,eff}}, \quad Bi = \frac{h_v \delta^2}{k_{s,eff}},$$

$$R_k = \frac{k_{f,eff}}{k_{s,eff}}, \quad Ec_1 = \frac{\alpha_1 \eta \delta}{k_{s,eff} (T_{f,in} - T_r) C_{O_2,ref}}, \quad \text{and}$$

$$Ec_2 = \frac{\alpha_2 \eta \delta}{k_{s,eff} (T_{f,in} - T_r) C^2_{H_2O,ref}}.$$

The dimensionless forms of the two-equation model thus become

$$0 = \frac{\partial^2 \theta_s}{\partial X^2} + \frac{\partial^2 \theta_s}{\partial Y^2} - Bi(\theta_s - \theta_f) \tag{38}$$

$$U \frac{\partial \theta_f}{\partial X} + V \frac{\partial \theta_f}{\partial Y} = \frac{1}{Re \cdot Pr_{eff}} \left(\frac{\partial^2 \theta_f}{\partial X^2} + \frac{\partial^2 \theta_f}{\partial Y^2} \right) + \frac{Bi}{RePr_{eff} R_k} (\theta_s - \theta_f) \tag{39}$$

The boundary conditions on the reaction surfaces are

$$\frac{\partial \theta_s}{\partial X} + R_k \frac{\partial \theta_f}{\partial X} + Ec_1 C_{O_2} - Ec_2 C^2_{H_2O} = 0 \tag{40}$$

$$\theta_f = \theta_s \tag{41}$$

It is noted that using a given interstitial heat transfer coefficient (h_v) together with the prescribed values of geometric properties, physical properties, measured inlet air temperatures, and a volumetric flow rate, the solid and fluid phase temperatures can be solved.

3.5. Charge transfer

The conservation of electric potential in the solid phase of the porous electrode can be expressed as

$$\frac{\partial^2 \phi_s}{\partial x^2} + \frac{\partial^2 \phi_s}{\partial y^2} = 0 \tag{42}$$

On the reaction surfaces, the electric potential gradient driving the current generated by the electrochemical reaction is

$$-\sigma_{s,eff} \frac{\partial \phi_s}{\partial x} = \alpha_1 \left(\frac{c_{O_2}}{c_{O_2,ref}} \right) - \alpha_2 \left(\frac{c_{H_2O}}{c_{H_2O,ref}} \right)^2 \tag{43}$$

Using the non-dimensional solid phase potential, $\Phi_s = \frac{F \phi_s}{RT_r}$, the above equations become

$$\frac{\partial^2 \Phi_s}{\partial X^2} + \frac{\partial^2 \Phi_s}{\partial Y^2} = 0 \tag{44}$$

$$\frac{\partial \Phi_s}{\partial X} = a_1 C_{O_2} - a_2 C^2_{H_2O} \tag{45}$$

where

$$a_1 = \frac{F \delta \alpha_1}{RT_r \sigma_{s,eff} C_{O_2,reff}}$$

and

$$a_2 = \frac{F \delta \alpha_2}{RT_r \sigma_{s,eff} C^2_{H_2O,ref}}$$

Conditions for the other boundaries of the present computational domain can be summarized as follows.

At the module inlet

$$P = P_{in}, \quad C_{O_2} = C_{O_2,in}, \quad C_{H_2O} = C_{H_2O,in},$$

$$\theta_f = \theta_{f,in}, \quad \frac{\partial \theta_s}{\partial X} = Bi(\theta_s - \theta_f), \quad \frac{\partial \Phi_s}{\partial X} = 0 \tag{46}$$

At the current collector surface

$$\frac{\partial P}{\partial X}=0,\quad U=V=0,\quad \theta_s=1,$$
$$\frac{\partial \theta_f}{\partial X}=\frac{Bi}{Pr_{eff}ReR_k}(\theta_s-\theta_f),\quad \Phi_s=0 \tag{47}$$

At the module outlet

$$P=P_{out},\quad \frac{\partial C_{O_2}}{\partial X}=\frac{\partial C_{H_2O}}{\partial X}=0,\quad \frac{\partial \theta_f}{\partial X}=0,$$
$$\frac{\partial \theta_s}{\partial X}=Bi(\theta_s-\theta_f),\quad \frac{\partial \Phi_s}{\partial X}=0 \tag{48}$$

3.6. Numerical methodology

The governing equations are numerically solved by the finite-element-based commercial code [27]. It uses the Broyden's method with an LU-decomposition pre-conditioner to solve the non-linear equations iteratively. A penalty term is employed for pressure to reduce continuity errors. Thus, there is a continuous part of the pressure and piecewise constant part providing and extra DOF (degree of freedom) for pressure on each element. It uses Newton–Raphson iteration to solve the close-coupled groups (velocity, pressure, temperature, concentration and electricity) and uses the frontal algorithm (Gaussian elimination) to solve the linearized system of equations for each iteration. Variable grids in the x-direction and uniform grids in the y-direction were employed in the present study [28]. Solutions are considered to be converged when all residual sources (including mass, momentum, temperature, species and charge) were less than 1.0×10^{-6}. A typical simulation requires about 60 min of central processing unit time on a Pentium IV 2.0 GHz PC.

4. Results and discussion

Before the discussion of the numerical results, it requires to validate the numerical model by comparing the present numerical results with the available experimental data. To this aim, the authors have made a comparison of the polarization curve between the numerical predictions with the experimental data under adiabatic conditions elsewhere [29]. The agreement for the comparison is acceptable, indicating that the results obtained by the present model are reliable.

4.1. Thermal-fluid fields

Fig. 3 shows the flow velocity vectors (composed by U and V) inside the porous electrode. The Reynolds number and Darcy number are fixed at $Re=10$ and $Da=9.8\times10^{-6}$, respectively. Two point indications in Fig. 3 represent the locations and values of the maximum and minimum velocities, respectively. It is seen from Fig. 3 that the velocity is higher in the core region between the rib surfaces and the reaction surfaces. In addition, due to the flow-turning

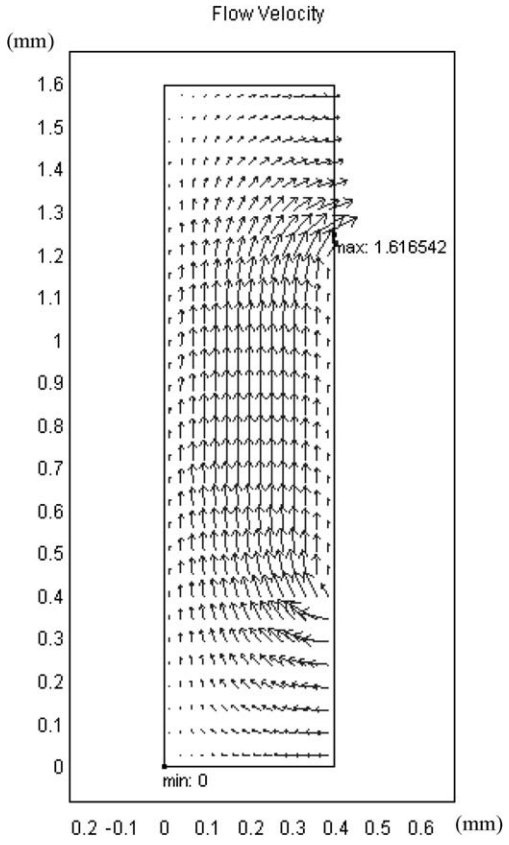

Fig. 3. Flow velocity distributions across the porous electrode, $Re=10$.

effect, the velocities around the bottom-left and top-left corners (i.e., the corners formed by two symmetric planes and the reaction surfaces) of the module are rather small. The small flow velocity weakens the forced convection, thus reduces the heat/mass transfer capability. It will be shown later.

Figs. 4(a) and 4(b) compare the distributions of the fluid-phase temperature (θ_f) and the solid-phase temperature (θ_s) in the porous electrode under various $\varepsilon RePr_{eff}R_k/Bi$. At Fig. 4(a), the flow parameters of interstitial heat transfer coefficient is assumed as $h_v=5.0\times10^5$, while the Reynolds number is fixed at $Re=10$. Using the typical values of Pr_{eff} and R_k shown in Table 1, the LNTE parameter $\varepsilon RePr_{eff}R_k/Bi$ becomes 0.548. Clearly, the temperature distributions are rather different between these two phases. The low and uniform fluid temperature from the inlet gradually increases as the flow approaching the ORR surfaces. The turning flow from the module inlet washes the reaction surface (Fig. 3), and thus results in a relatively low temperature on in the middle region near the reaction surfaces (about $Y=0.7$–0.9). The local maximum fluid-phase temperatures occur at the abovementioned two corners where the fluid is nearly stagnant (Fig. 3). As for the solid-phase temperature, the temperature gradients near the isothermal rib surfaces are significant. The isothermal rib acts as a heat sink to absorb the heat generated by the ORR on the reaction surfaces. Similarly, the local maximum solid-phase

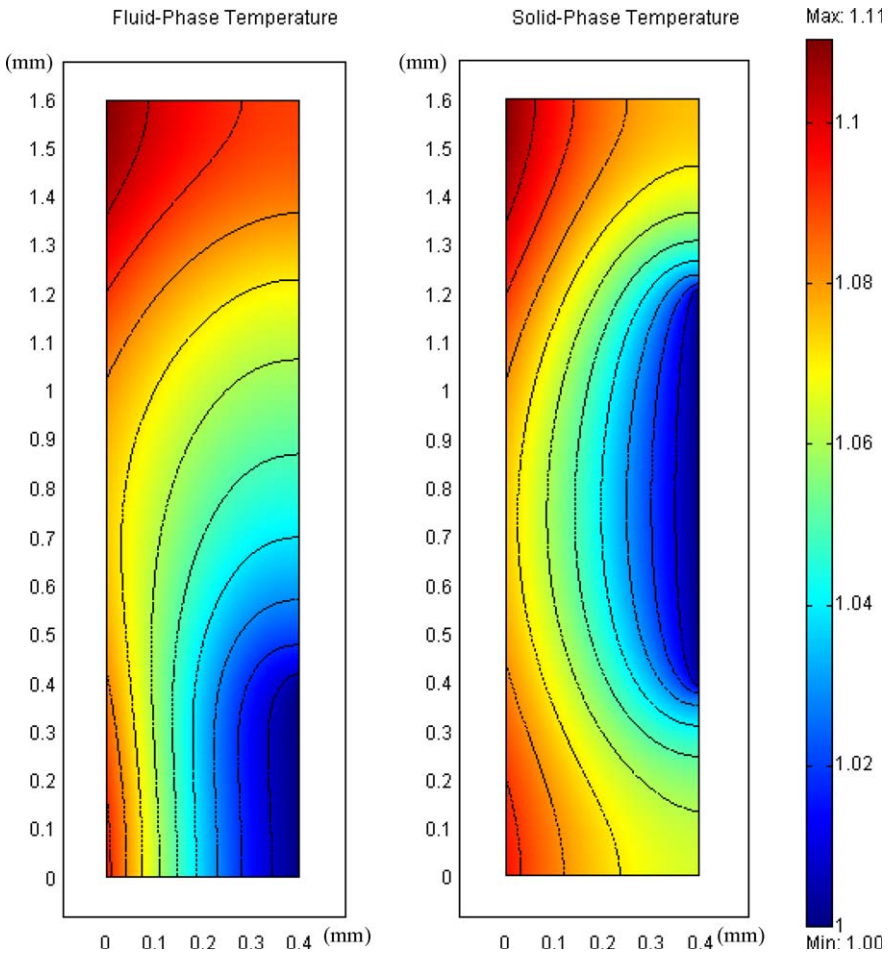

Fig. 4(a). Comparison of fluid-phase and solid-phase temperature distributions inside the porous electrode for $Re = 10$, and $\varepsilon Pr_{\text{eff}} Re R_k/Bi = 0.548$.

temperatures occur at two corners formed by the two symmetric planes and the reaction surfaces.

As the parameter $\varepsilon Re Pr_{\text{eff}} R_k/Bi$ decreases to 2.74×10^{-3}, as shown in Fig. 4(b), the temperature distributions between the solid phase and fluid phase do not different two much. The most significant difference occurs near the module inlet where the uniform inlet fluid temperature is lower than the solid one, meaning that the heat is transferred from the solid to the fluid. A large similarity in the temperature distribution between the solid phase and fluid phase gives an indication that the thermal-fluid field in the porous electrode has approached the local thermal equilibrium.

Fig. 5(a) and (b) shows the heat flux across the fluid phase and solid phase of the porous electrode, respectively. The Reynolds number and LNTE parameter are fixed at $Re = 10$. $\varepsilon Re Pr_{\text{eff}} R_k/Bi = 0.548$, respectively. The point indications shown in each plot mean the locations and values of the maximum or minimum heat fluxes. In the fluid phase, the heat is carried by the fluid, and thus the convection dominates the heat transfer mechanisms. Therefore, the patterns of heat-flux vectors (Fig. 5(a)) are largely similar to those of the velocity vectors in the fluid-flow field (Fig. 3). In contrast, the heat traverses the solid matrix of the porous electrode mainly by conduction. The heat-flux vectors direct from the reaction surfaces toward the isothermal rib surfaces. The maximum conductive heat flux occurs at the surfaces attached to the rib upper corner.

4.2. Wall heat flux and Nusselt number

Fig. 6 shows the wall heat flux along the ORR surfaces ($X = 0$). The heat generated by the ORR on the reaction surfaces is transferred either by the solid or by the fluid. The non-dimensional heat flux through the solid and fluid phases on the reaction surfaces can be represented by $Q_s = -\left(\frac{\partial \theta_s}{\partial X}\right)_w$ and $Q_f = -R_k\left(\frac{\partial \theta_f}{\partial X}\right)_w$, respectively. It is seen that the heat transfer by the solid-phase conduction on the reaction wall is greatly higher than that by the fluid phase. This is because the significantly higher thermal conductivity of the solid phase (Table 1) can provide a wider thermal pathway for channeling out the heat. It is further seen that the total wall heat flux decreases with increasing Y. This is because the heat generation by electrochemical reaction is reduced due to the decrease in the oxygen concentration along the Y direction, which will be shown later.

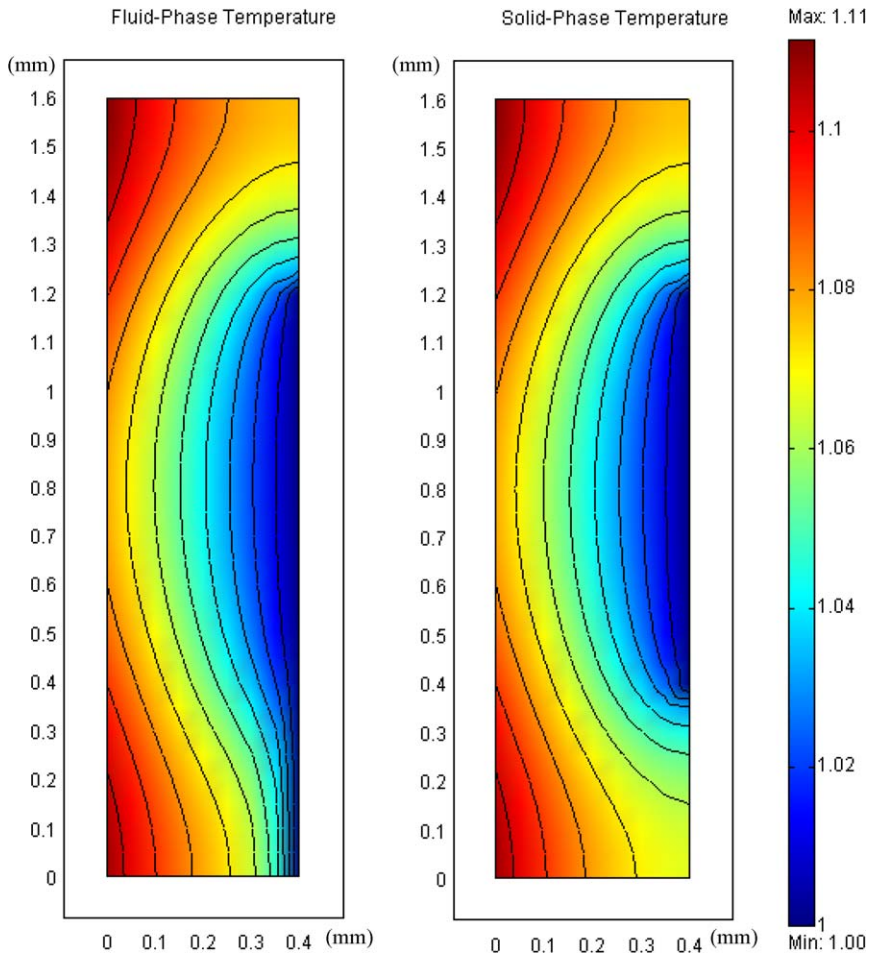

Fig. 4(b). Comparison of fluid-phase and solid-phase temperature distributions inside the porous electrode for $Re = 10$, $\varepsilon Pr_{\text{eff}} Re R_k/Bi = 2.74 \times 10^{-3}$.

Fig. 7 shows the distributions of wall temperature and Nusselt number on the reaction surfaces. It is seen that the wall temperature decreases to a local minimum at about $y = 0.8$ mm and then increases to a local maximum at $y = 1.6$ mm. It is reasonable because the region of local minimum temperature faces the cold rib surfaces, and thus has a shorter distance to transfer the heat from the hot reaction wall to the cold rib surfaces. In addition, the washing effect by the cold turning flow, to a certain extent, reduces the wall temperature.

The Nusselt number on the reaction surfaces can be defined as the ratio of heat dissipation from the reaction surface to the temperature difference, i.e.,

$$Nu = \frac{q_w \delta}{k_f (T_{f,in} - T_r)} = \frac{\left(-k_{s,\text{eff}} \dfrac{\partial T_s}{\partial x} - k_{f,\text{eff}} \dfrac{\partial T_f}{\partial x} \right)_w \delta}{k_f (T_{f,in} - T_r)} = -\frac{k_{f,\text{eff}}}{k_f} \left(\frac{1}{R_k} \frac{\partial \theta_s}{\partial X} + \frac{\partial \theta_f}{\partial X} \right)_w \quad (49)$$

Since $k_{f,\text{eff}} = \varepsilon k_f$, therefore the above equation can be further reduced to

$$Nu = -\varepsilon \left(\frac{1}{R_k} \frac{\partial \theta_s}{\partial X} + \frac{\partial \theta_f}{\partial X} \right)_w \quad (50)$$

It is seen from Fig. 7, the Nusselt numbers on the reaction surfaces range from 5.10 to 5.36. The maximum Nu occurs at $Y = 0.6$. In general, the Nu distribution has an adverse trend as that of wall temperature on the reaction surfaces.

4.3. Concentration distributions

Fig. 8(a) and (b) shows the oxygen and water–vapor concentration distributions in the porous electrode, respectively. The composition of the oxygen–water vapor mixture at the module inlet is $C_{O_2} = 0.9$ and $C_{H_2O} = 0.1$. The Reynolds number and LTNE parameter are fixed $Re = 10$ and $\varepsilon Re Pr_{\text{eff}} R_k/Bi = 0.548$, respectively. The development of oxygen concentration distribution is closely related to the flow evolution shown in Fig. 3. It is seen that high-concentrated oxygen from the entrance of the module decreases as the flow approaches the reaction surfaces and moves downstream. The lowest values of C_{O_2} are found in upper corner adjacent the reaction surfaces. In this region, some oxygen has been depleted by the upstream reaction, and the stagnant fluid (Fig. 3) cannot refresh the oxygen. It is further seen from Fig. 8(b) that the C_{H_2O} distributions just compensate for those of C_{O_2}. It increases along the flow

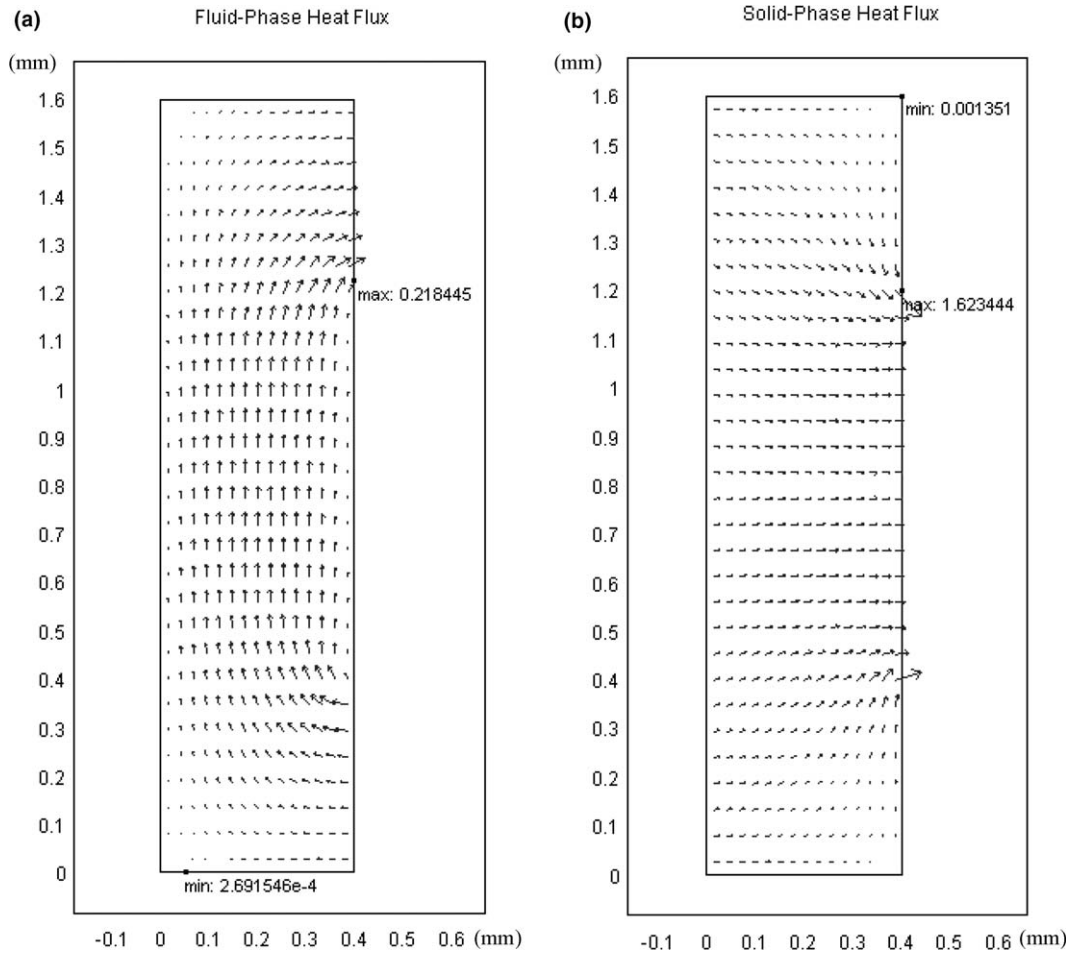

Fig. 5. Comparison of the heat flux across the solid phase and fluid phase of the porous electrode, $Re = 10$, and $\varepsilon Pr_{\text{eff}} ReR_k/Bi = 0.548$.

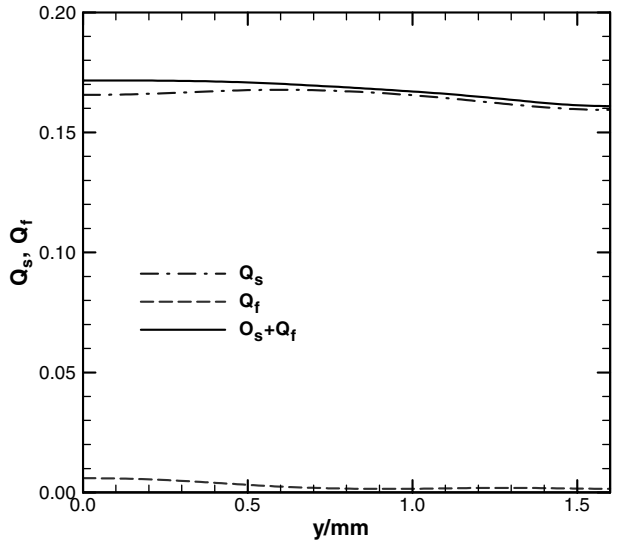

Fig. 6. Heat fluxes across the fluid phase and solid phase on the reaction surfaces ($X = 0$), $Re = 10$, and $\varepsilon Pr_{\text{eff}} ReR_k/Bi = 0.548$.

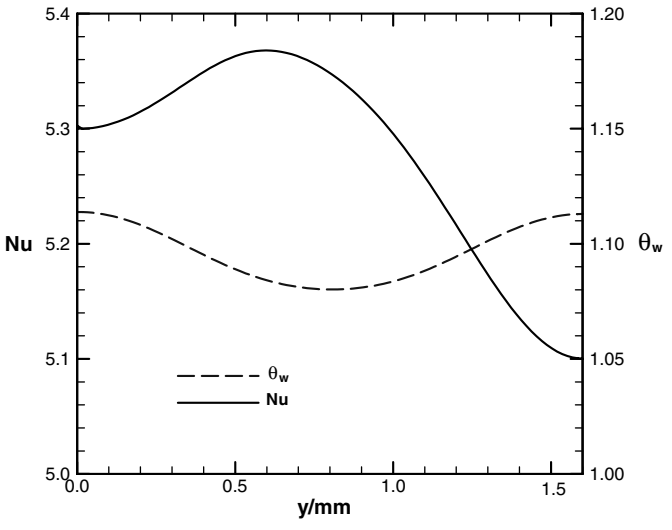

Fig. 7. Wall temperature and Nusselt number distributions along the reaction surfaces ($X = 0$), $Re = 10$, and $\varepsilon Pr_{\text{eff}} ReR_k/Bi = 0.548$.

direction due to the convective accumulation downstream of the water vapor generated on the ORR surfaces (Eq. (12)).

Fig. 9 shows the oxygen and water vapor concentrations distribution along the reaction surfaces ($X = 0$). It is seen

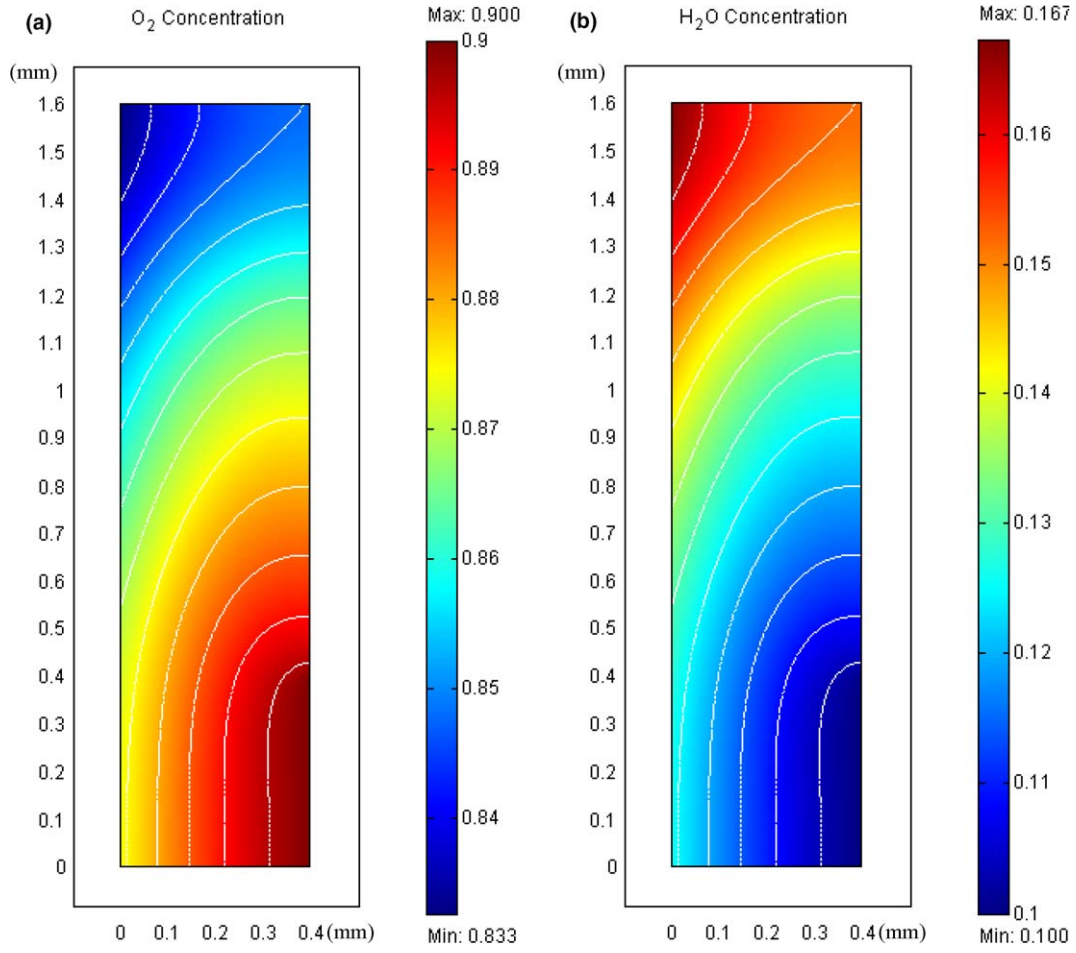

Fig. 8. Concentration distributions of O_2 and H_2O in the porous electrode, $Re = 10$, and $\varepsilon Pr_{\text{eff}} Re R_k / Bi = 0.548$.

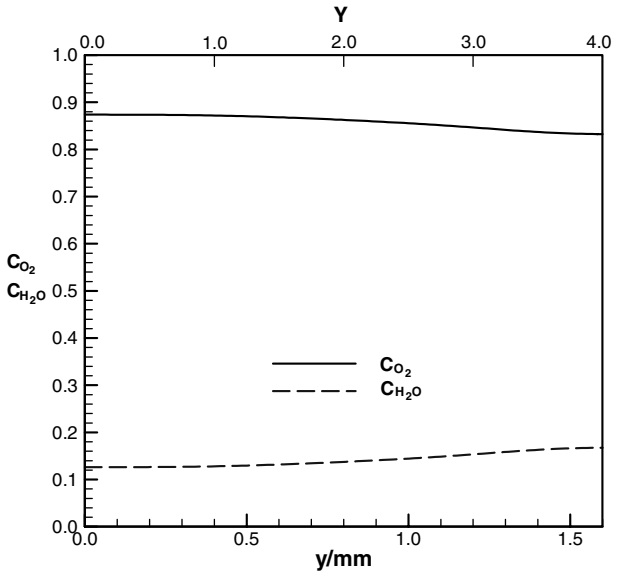

Fig. 9. Species concentration distributions along the reaction surfaces, $Re = 10$, and $\varepsilon Pr_{\text{eff}} Re R_k / Bi = 0.548$.

that the oxygen/water vapor concentrations decreases/increases along the Y direction due to the ORR on the reaction surface. The decrease in the oxygen concentration results in the decrease of heat generation on the reaction surfaces (Fig. 6).

4.4. Electric fields

Fig. 10 shows the current density as well as the electric potential distributions within the module. The current–density vectors are heading for the rib surfaces. The arrows indicate the direction and the magnitude of the current density. It is seen that both current density and the electric potential distribution are roughly symmetric about the mid-plane of the module ($Y = 0.8$). Because the electric properties employed are thermally independent, the electric field in the porous electrode does not affect by the thermal-fluid fields in essential. The only way to modify the electric field is to alter the reactant concentrations on the reaction surfaces by electrochemical reactions (Eq. (45)).

5. Conclusions

A multi-physics model coupling heat/mass transfer with electrochemical kinetics has been performed to simulate the transport phenomena inside the porous electrode of a

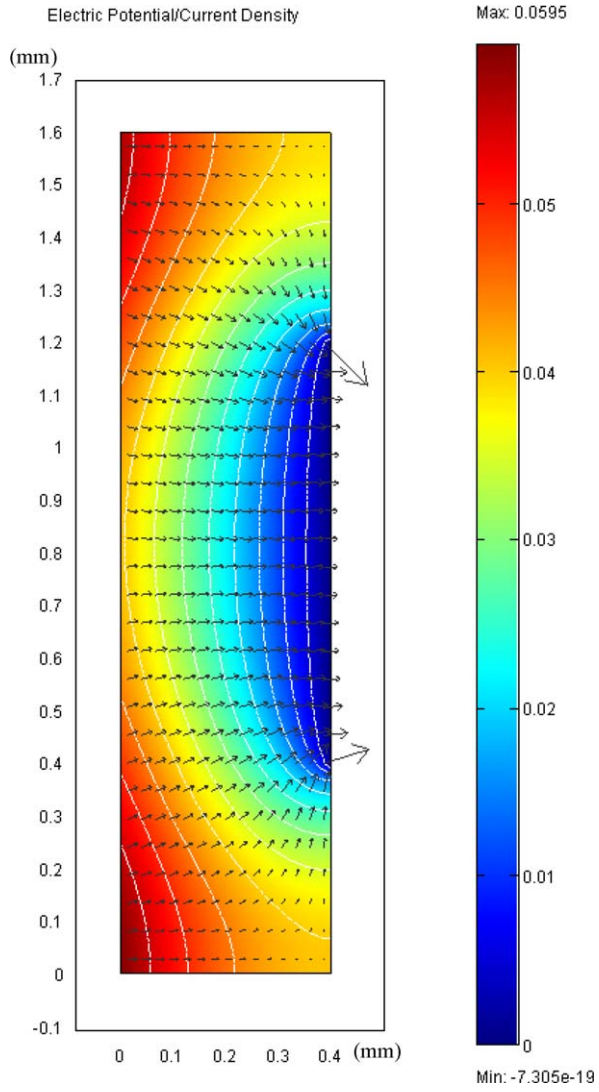

Fig. 10. Electric potential and current density distribution in the porous electrode, $Re = 10$, and $\varepsilon Pr_{\text{eff}} Re R_k/Bi = 0.548$.

low-temperature fuel cell. The unique features of this model are the first implementation of the local thermal non-equilibrium model coupled with the reactant concentration field which allows for a more realistic variation of the thermal-fluid and electrochemical kinetics in the porous electrode of fuel cells. In addition, the local thermal non-equilibrium characteristics of a typical porous electrode of fuel cells have been verified by using the LTNE parameter $\varepsilon Re Pr_{\text{eff}} R_k/Bi$ for the first time. It is found that as the LTNE parameter $\varepsilon Re Pr_{\text{eff}} R_k/Bi$ approach unit, the local thermal non-equilibrium becomes significant. Moreover, this model is capable of providing a cost-effective tool to accurately predict the cell thermal-fluid and electrochemical behaviors, such as flow velocities, reactant concentrations and current densities in the porous electrode of fuel cells. Most important, the heat/mass transfer mechanisms together with the thermal pathways in the fuel cell have been clearly identified. It would be beneficial for further accurate analyses of the fuel-cell thermal performance by considering the temperature-dependent physical properties inside the fuel cell.

Acknowledgement

This work was partly sponsored by the National Science Council of the Taiwan, ROC under contract No. NSC 92-2212-E-451-002.

References

[1] J.J. Hwang, D.Y. Wang, N.C. Shih, Development of a lightweight fuel cell vehicle, J. Power Sources 141 (2005) 108–115.
[2] J.J. Hwang, H.S. Hwang, Parametric studies of a double-cell stack of PEMFC using Grafoil flow-field plates, J. Power Sources 104 (2002) 24–32.
[3] D.M. Bernardi, M.W. Verbrugge, Mathematical model of a gas diffusion electrode bonded to a polymer electrolyte, Am. Inst. Chem. Eng. J. 37 (1991) 1151–1163.
[4] T.E. Springer, T.A. Zawodzinski, S. Gottesfeld, Polymer electrolyte fuel cell model, J. Electrochem. Soc. 138 (8) (1991) 2334–2342.
[5] T.V. Nguyen, R.E. White, A water and heat management model for proton-exchange-membrane fuel cells, J. Electrochem. Soc. 140 (8) (1993) 2178–2186.
[6] T.J. Jen, T. Yan, S.H. Chan, Chemical reacting transport phenomena in a PEM fuel cell, Int. J. Heat Mass Transfer 46 (2003) 4157–4168.
[7] J.S. Yi, T.V. Nguyen, An along-the channel model for proton exchange membrane fuel cells, J. Electrochem. Soc. 145 (4) (1998) 1149–1159.
[8] S. Dutta, S. Shimpalee, J.W. Van Zee, Numerical prediction of mass-exchange between cathode and anode channels in a PEM fuel cell, Int. J. Heat Mass Transfer 44 (2001) 2029–2042.
[9] H. Ju, C.Y. Wang, Experimental validation of a PEM fuel cell model by current distribution data, J. Electrochem. Soc. 151 (2004) A1954–A1960.
[10] S. Um, C.Y. Wang, Three-dimensional analysis of transport and electrochemical reactions in polymer electrolyte fuel cells, J. Power Sources 125 (2004) 40–51.
[11] L. You, H. Liu, A two-phase flow and transport model for the cathode of PEM fuel cells, Int. J. Heat Mass Transfer 45 (2002) 2277–2287.
[12] T. Ackmann, L.G.J. de Haart, W. Lehnert, D. Stolten, Modeling of mass and heat transport in planar substrate type SOFCs, J. Electrochem. Soc. 150 (2003) A783–A789.
[13] J. Yuan, M. Rokni, B. Sunden, Three-dimensional computational analysis of gas and heat transport phenomena in ducts relevant for anode-supported solid oxide fuel cells, Int. J. Heat Mass Transfer 46 (2003) 809–821.
[14] M. Quintard, S. Whitaker, Theoretical modeling of transport in porous media, in: K. Vafai (Ed.), Handbook of Heat Transfer in Porous Media, first ed., M. Decker, New York, 2000 (Chapter 1).
[15] M. Quintard, S. Whitaker, Local thermal equilibrium for transient heat conduction: theory and comparison with numerical experiments, Int. J. Heat Mass Transfer 38 (1995) 2779–2796.
[16] M. Sahraoui, M. Kaviany, Slip and no-slip temperature boundary condition at the interface of porous, plain media: convection, Int. J. Heat Mass Transfer 37 (1994) 1029–1044.
[17] J.J. Hwang, Thermal-electrochemical modeling of a proton exchange membrane fuel cell, J. Electrochem. Soc. 153 (2006) A126–A224.
[18] M. Kaviany, Principles of Heat Transfer in Porous Media, second ed., Springer, Berlin, 1995 (Chapter 3).
[19] J.J. Hwang, G.J. Hwang, R.H. Yeh, C.H. Chao, Measurement of interstitial convective heat transfer and fictional drag for flow across metal foams, J. Heat Transfer 124 (2002) 120–129.
[20] S.J. Kim, S.P. Jang, Effects of the Darcy number, the Prandtl number, and the Reynolds number on local thermal non-equilibrium, Int. J. Heat Mass Transfer 45 (2002) 3885–3896.

[21] T.E. Springer, T.A. Zawodzinski, S. Gottesfeld, Polymer electrolyte fuel cell model, J. Electrochem. Soc. 138 (1991) 2334–2341.
[22] J.J. Hwang, C.K. Chen, R.F. Savinell, C.C. Liu, J. Wainright, A three-dimensional numerical simulation of the transport phenomena in the cathodic side of a PEMFC, J. Appl. Electrochem. 34 (2004) 217–224.
[23] R.E. Meredith, C.W. Tobias, in: C.W. Tobias (Ed.), Advances in Electrochemistry and Electrochemical Engineering 2, Interscience Publishers, New York, 1962.
[24] H. Oldham, J. Myland, Fundamentals of Electrochemical Science, Academic Press, Inc., 1994.
[25] D.M. Bernardi, M.W. Verbrugge, Mathematical model of the solid–polymer-electrolyte fuel cell, J. Electrochem. Soc. 139 (1992) 2477–2491.
[26] L. Rao, J. Newman, Heat-generation rate and general energy-balance for insertion battery systems, J. Electrochem. Soc. 144 (1997) 2697–2704.
[27] J.J. Hwang, C.K. Chen, D.Y. Lai, Computational analysis of species transport and electrochemical characteristics of a MOLB-type SOFC, J. Power Sources 140 (2005) 235–242.
[28] J.J. Hwang, T.Y. Lia, S.H. Chen, Predictions of turbulent fluid flow and heat transfer in a rotating periodical two-pass square duct, Int. J. Num. Methods for Heat Fluid Flow 8 (1998) 519–538.
[29] J.J. Hwang, K.H. Lo, S.H. Wang, K.C. Tsay, Fuel cell dynamics and transport phenomena in a PEMFC, in: Proceedings of the 25th Conference on Theoretical and Applied Mechanics, Taichung, Taiwan, 2001, pp. 3611–3620 (in Chinese).